Bottom-Up Exploration: Imaging Resistivity of a Mineral System from Source to Sink

Thesis submitted in accordance with the requirements of the University of Adelaide for an Honours Degree in Geophysics.

Emily Lewis

November 2021

THE UNIVERSITY of ADELAIDE

BOTTOM-UP EXPLORATION: IMAGING ELECTRICAL RESISTIVITY OF A MINERAL SYSTEM FROM SOURCE TO SINK

ELECTRICAL RESISTIVITY OF A MINERAL SYSTEM

ABSTRACT

Ore deposits are broadly defined as a geochemical anomaly which has been concentrated from a significantly larger volume source at depth. This requires a mineral system process through which elements in the lower crust or mantle are entrained and moved to the surface. In various locations around the world, the source region of a mineral system has been shown to have a distinct electrical resistivity signature as a result of past magmatic fluid processes which have left a geochemical overprint. This project focuses on the Curnamona Province, a Paleo-Mesoproterozoic craton which extends across South Australia and New South Wales with approximate dimensions of 300 km east-west and 300 km north-south. A previous broadband magnetotelluric (MT) (10^2 to 0.01 Hz) traverse of 60 stations spaced 2 km across the Curnamona Province identified a 2D geophysical signature with a footprint similar to that below the IOCG Olympic Dam deposit in the Gawler Craton. In this project, broadband MT measurements (10^4 to 0.01 Hz) were collected along four parallel lines of 1 km spaced sites, and with line separation of 5 km to develop the 3D context. We image a discrete low-resistivity zone on three of the lines, which extends from the surface down to 20 km depth, where it is linked to a conductor of 1Ωm. It appears to be bound between two resistive blocks and is not laterally continuous. The outcomes of this model are comparable to pathways across the Gawler Craton. We show a very strong relationship between deep crustal conductors and narrow pathways, inferring a signature which is responding to past magmatic events.

KEYWORDS

Magnetotellurics, electrical resistivity signature, mineral system

TABLE OF CONTENTS

Bottom-Up Exploration: Imaging Electrical Resistivity of a Mineral System from Source to Sink i
Electrical Resistivity of a Mineral System i
Abstract i
Keywords i
List of Figures and Tables 2
Introduction 4
Background 5
Geological setting 5
Previous Geophysical Surveys 8
Methods 11
MT Theory 11
Survey 13
Results 15
Data quality 15
3-D model 16
2-Dimensional Regional Model 18
2-Dimensional Jupiter Models 19
1-D Batch inversions 20
Discussion 22
Conclusions 35
Acknowledgments 35
References 36
Appendix A: 3D Model Set up and fits 38
Appendix B: 2-D regional model set up 39
Appendix c: 2-D Jupiter profile models 41
Appendix D: 1-D model set up 42

LIST OF FIGURES AND TABLES

Figure 1: Location map of the Curnamona Province, illustrating the boundaries of its eight domains. 2021 broadband MT sites are denoted by white triangles and 2017 Curnamona Conductor (CC) sites in black. Major mines within the region are represented by a red diamond. Solid Geology boundaries are adapted from adapted from Wade et al. (2012) and Armistead et al. (2018). 7
Figure 2: a) CCMT 2017 stations (red triangles) and 2021 Jupiter MT stations (black triangles) with regional Curnamona Cube MT stations as blue dots, overlain by gridded potential field magnetic dataset. b) Contour map of depth to basement in metres relative to sea level. c) Ground level gravity in m/s^2. d) Elevation map over the same area represented in metres above sea level. e) Aerial Electromagnetic (AEM) data averaged over the upper 100 m. f) 2-D cross section model to ~35km depth from CCMT_2017 transect, as per (Kay et al. 2021). 11
Figure 3: phase tensors skew (β) angle up to 100 seconds along a) profile A, b) profile B, c) profile C, d) profile D. Black triangles represent MT stations from 2021, while red triangles are from the 2017 CCMT transect. The black dashed line represents the point along each profile where the skew angle becomes $>5^o$, and thus is considered to have 3D structure. 16
Figure 4: 3-D inversion model depth slice at a) 500m, b) 2km c) 10km, d) 20km. Note the black outline represents the extent of Lake Frome, red triangles are 2017 CCMT stations, black triangles are Jupiter MT stations and blue circles are MT stations from the regional Curnamona Cube project. 17
Figure 5: 2-D cross sectional model of Jupiter profile C (black triangles), extending 100km to include 2017 CC MT stations (red triangles). Conductive features C1 occurs at ~15-30km depth and C2 5-20km depth. Of particular interest are the regions which exist between resistive blocks labelled R1, R2 and R3. 19
Figure 6: 2-dimensional cross sections for the upper 25km along profiles a, b c & d. The same scale bar is used for all models, a conductive region C1 (<1Ωm) is imaged in profiles a, b, and c, but is absent in d. C2 represents a low resistivity pathway between resistive blocks R1 & R2. 20
Figure 7: 1-D inversion of MT data depth slices at a) 500 m, b) 2 km, c) 10 km and d) 20 km. C1 has been labelled to highlight the persistent conductive structure in between two resistive (R1 & R2) blocks. Easting and Northing are given in km are using WGS 84, UTM Zone 54S. 22
Figure 8: a) AEM depth slice from 80-90 m. Note the MT stations and profiles are only for reference locations and the data is independent of these sites. The grey horizontal lines present the flight path of 2.5 km spacing. b) 1-D MT batch inversion at 80m, showing a similar resistive region over the South-Eastern portion of the array as well as conductive anomaly along profile C. 24
Figure 9: Bootstrap model of the logarithmic mean of profile C, including CCMT_2017 stations 06-26 and Jupiter C1-9. It shows a relatively conductive pathway from the upper crust to a depth of ~15km. This provides confidence in the model presented in figure 3, as this feature, although weak is statistically present in the data. Notably, the conductive region at ~15km depth also appears to be much weaker and ~10Ωm instead of 1 Ωm presented in figure 6c. 26

Figure 10: bootstrap model of the percentage deviation for each cell within the model. Zero represents no doubt in the structure, while 100 indicates no confidence that the feature exists within the electrical resistivity structure. 27
Figure 11: a) 2-D resistivity model of the Gawler Craton to 30km depth. WW, OD, and VC represent major mineral deposits Wirrida Well, Olympic Dam, and Vulcan. b) regional 2-D resistivity model over the Curnamona Province. Note this is the same model as in figure 5 but focusses on a smaller linear scale and reduced colour scale. .. 30
Figure 12: a) 1D batch inversion models of Jupiter site at 5 km depth. b) depth slice at 10 km. c) Separate 1D inversion surrounding Carrapateena IOCG mine (red diamond), at 5 km depth. d) depth slice at 10 km. Both models show similarities with a sub-circular feature surrounded by comparatively resistive material. Notably, Carrapateena does not sit on top of this structure, but exists ~5Km to the S-E. 31

INTRODUCTION

A major restriction to mineral exploration within Australia is from limited outcrop due to thick sediment cover (Robertson and Thiel 2019). Recent developments in the mineral systems approach have guided the focus of exploration on understanding how fluid flow is organised in the crust (McCuaig and Hronsky 2014). As a result, geophysical techniques including MT have become a useful means of exploration targeting, by providing insight on the whole lithosphere architecture (Armistead et al. 2018).

MT is a geophysical technique which involves simultaneously measuring the Earth's time-varying natural magnetic and electric fields. By calculating the complex ratio (impedance) of variation in these fields, the electrical resistivity structure below the Earth's surface can be interpreted ranging up to several hundred kilometres depth (Simpson and Bahr 2005). Within the Curnamona Province, MT has been used to image the crust with varying degrees of resolution (Robertson et al. 2016, Milligan and Lilley 2010, Wang et al. 1997). Specifically, a large linear low-resistivity feature dubbed the 'Curnamona Conductor' has been observed at ~5-40 km depth (Robertson et al. 2016).

Large upper crustal linear conductors such as this are not exclusive to the Curnamona Province, with numerous similar features having been identified worldwide (Selway 2014). Notably, there are several examples of these, which occur along the transition from Archean to Paleoproterozoic craton boundaries (Boerner et al. 1996), as is the case with the Curnamona Conductor. Also included within this category are the Carpentaria Conductor in Queensland and the Northern American Plains Anomaly (Jiang et al.

2019). This is significant as Mesoproterozoic plate reconstructions provide a spatial link to both the Mount Isa inlier and Wernecke Mountains in Canada (Thorkelson et al. 2001, Page et al. 2005). During this period, it is suggested that mantle plume activity was the driver for a major tectono-thermal event which caused hydrothermal alteration and Cu-Au mineralisation (Conor and Preiss 2008).

The most favourable mechanism for the formation of this feature involves interconnected graphite grains growing along boundaries, as a result of deformation processes metamorphosing organic Carbon (Kay et al. 2021). This paper focusses on the Curnamona Conductor as identified by (Robertson et al. 2016), hypothesising that the electrical resistivity structure of the crust and upper mantle can be used to define a mineral system from source regions to the sink. This is based on the sub hypothesis that a mineral system has a distinct electrical resistivity signature, which can be attributed to past fluid and thermal processes. This has been shown in a similar case study at the Olympic Dam IOCG-U deposit in South Australia (Heinson et al. 2018a).
This study will evaluate data new MT data from the Curnamona Province and compare to previous models as per (Kay 2017, Kay et al. 2021, Robertson et al. 2016).

BACKGROUND

Geological setting

The Curnamona Province is a Paleo-Mesoproterozoic domain within the Eastern portion of South Australia and Western New South Wales (Myers et al. 1996). It is separated from the Gawler Craton by the Ikara-Flinders Ranges and delineated by a unique magnetic signature as a result of Neoproterozoic and Palaeozoic tectonic events (Conor

and Preiss 2008). It can be split into eight sub-domains, as per figure one; based off sedimentary facies, tectonic volcanic and metamorphic characteristics. The Willyama Supergroup makes up the basement rocks for this domain and are suggested to have formed after crustal extension, during a phase of basin formation lasting at least 80 Ma, from ~1720 to 1640 Ma (Conor and Preiss 2008). Much of its extent is concealed by Neoproterozoic- Quaternary sedimentary cover, with outcrop limited to the Willyama Inlier in the South, and Mount Painter and Mount Babbage Inliers in the North (Dentith et al. 2003). All other geological boundaries have been interpreted primarily through drilling programs in conjunction with geophysical surveys (Wade 2011, Dentith et al. 2003).

The area of focus for this project is centred over the Mudguard Domain, but also includes an Eastern portion of the Moorowie Sub-basin / Erudina Domain. The stratigraphy of this area is dominated by the magmatic Ninnerie Supersuite, which intruded the Willyama Supergroup from ~1600-1570 Ma, as a result of the concluding stages of the Olarian orogeny (Wade et al. 2012). Included within the Ninnerie Supergroup is the ~1587-1581 Ma Benagerie Volcanic Suite. This is comprised of generally A type volcanic and sub-volcanic rocks (Wade 2011) and has been mapped as a separate unit in figure one. Notably, the bimodal magmatic emplacement of the Ninnerie Supergroup within the Curnamona was contemporaneous with the Hiltaba Suite granites and Gawler Range Volcanics of the Gawler Craton (Wade et al. 2012).

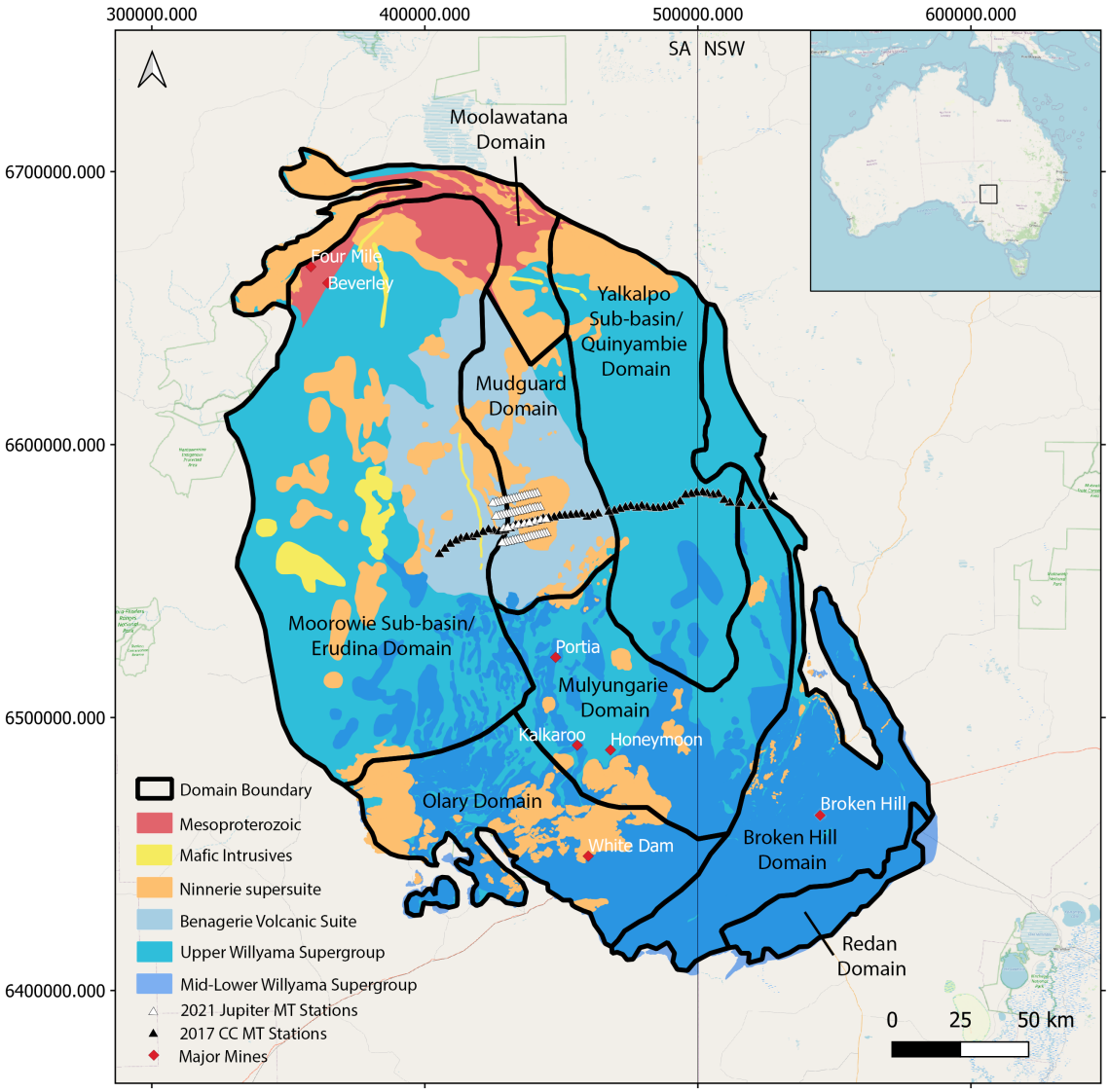

The Curnamona Province is host to the Broken Hill Pb-Zn-Ag-(Au) lode as well as several smaller Cu-Au-Mo deposits (Conor and Preiss 2008). Notably, major mines including Kalkaroo, Honeymooon and Portia occur on the stratigraphical boundary between the upper and mid Willyama Supergroup (Leyh and Conor 2000). This is likely due to the presence of the sulphidic Bimba Suite, which has been suggested as a

structurally controlled redox boundary, playing an important role in base-metal mineralisation within the Olary and Broken Hill Domains.

Despite this, the extensive sedimentary cover inhibits knowledge of the location of this this stratigraphic horizon, over the Mudguard Domain. Consequently, structural controls on mineral systems are poorly constrained within the area of interest for this project. The Benagerie shear zone is one such feature which may influence mineral system. Running directly adjacent to the area of interest, this is a deeply rooted, large scale feature with a ~1100 Ma history playing a causal role in the emplacement of the Ninnerie Supersuite (Williams and Betts 2009). This has been identified through a combination of field studies and geophysical methods, manifesting as a 10-20km wide corridor in the Benagerie Volcanic Province (Williams and Betts 2009).

Previous Geophysical Surveys

Electrical Resistivity models using the MT method across the Gawler Craton in South Australia have identified a distinct signature of a magmatic mineral system, associated with emplacement of iron-oxide copper gold uranium (IOCG-U) deposits (Heinson et al. 2018a). In this 2-D resistivity model, three narrow low resistivity fluid pathways extending from a broader conductive region at ~15km depth, to the base of the sedimentary layer are imaged. Each of these regions coincide with a comparatively thin cover sequence, suggesting rheological weakness in the crust, despite no significant mapped crustal scale faults. Moreover, these pathways are also coincident with the major deposits along the transect, including Olympic Dam, Wirrda Well and Vulcan (Heinson et al. 2018a).

Looking specifically at the Curnamona Province, a considerable conducting region was first identified and termed the 'Flinders Conductive Anomaly' in 1972 (Gough et al. 1972). This was further delineated by numerous studies over the years, suggesting a single continuous conductor over 400km in length (Milligan and Lilley 2010, Tammemagi and Lilley 1973, Chamalaun 1985). The Australian Lithospheric Architecture Magnetotelluric Program (AusLAMP), an array of ~55 km spaced long-period MT sites noted that this feature was in fact two separate features – the Curnamona Conductor and Eastern Nackara Arc Conductor, which are attributed to discrete tectonic events. Of particular interest is the 'Eastern Nackara Arc Conductor', which is situated at the approximate location of the transition from Proterozoic to Phanerozoic lithosphere (Robertson et al. 2016). This signature is suggested to represent pathways which once stemmed down to the lower mantle, depositing a conductive phase during the ascent of partial melt or fluid. This is evidenced by the presence of diamondiferous kimberlites in this region which broadly align with Eastern Nackera Arc conductors (Robertson et al. 2016).

While the Curnamona Conductor was broadly defined, the AusLAMP survey was designed for terrain investigation and hence the anomaly lacked resolution at mid-upper crustal levels. To further delineate this conductive feature, a MT transect of 2 km site spacing was completed across strike (Kay et al. 2021, Kay 2017). This identified numerous features including a conductive anomaly (1 Ωm) at ~20 km depth, with a pathway of 100 Ωm extending upwards to a topographical basement high. The 2-D cross sectional model from this transect is presented in figure two f.

Potential field data provide an understanding of density and magnetic variations and have been presented in figure two a, and c**.** The most significant feature within the magnetic data is a high magnetic anomaly (up to 1000 nT), to the East of the array. The area over the array itself is relatively homogenous in comparison, ranging from 400 – 700 nT. The gravity data appears to follow a similar trend to the elevation contours, which are shown in figure two, d. The gravity data presents a decrease in gravitational acceleration around the central Northern area of the array. This suggests an increase in density of the Earth's crust towards the south and edges, shown in figure two c. Note both the magnetic line spacing and gridded gravity datasets are quite broad and more suitable for regional interpretations, with the resolution inadequate to image smaller scale features. Depth to base of Cenozoic sediments is presented in figure two b. This highlights a topographic high over the array, particularly around the more southern profiles.

Airborne Electromagnetic (AEM) data acquired by Geoscience Australia through the Frome Embayment AEM survey, was designed to reveal new geological information at a regional scale, at a flight spacing of 2.5 km (Roach 2012). The depth of investigation (DOI), deemed as the depth of reliable penetration for this area was 100 m. While this dataset presents a model of the electrical resistivity structure to this DOI, it does not image to lower crustal depths. Thus, is useful to correlate models at near surface depths, but not practical beyond, hence the average of the upper 100m is presented in figure two, e.

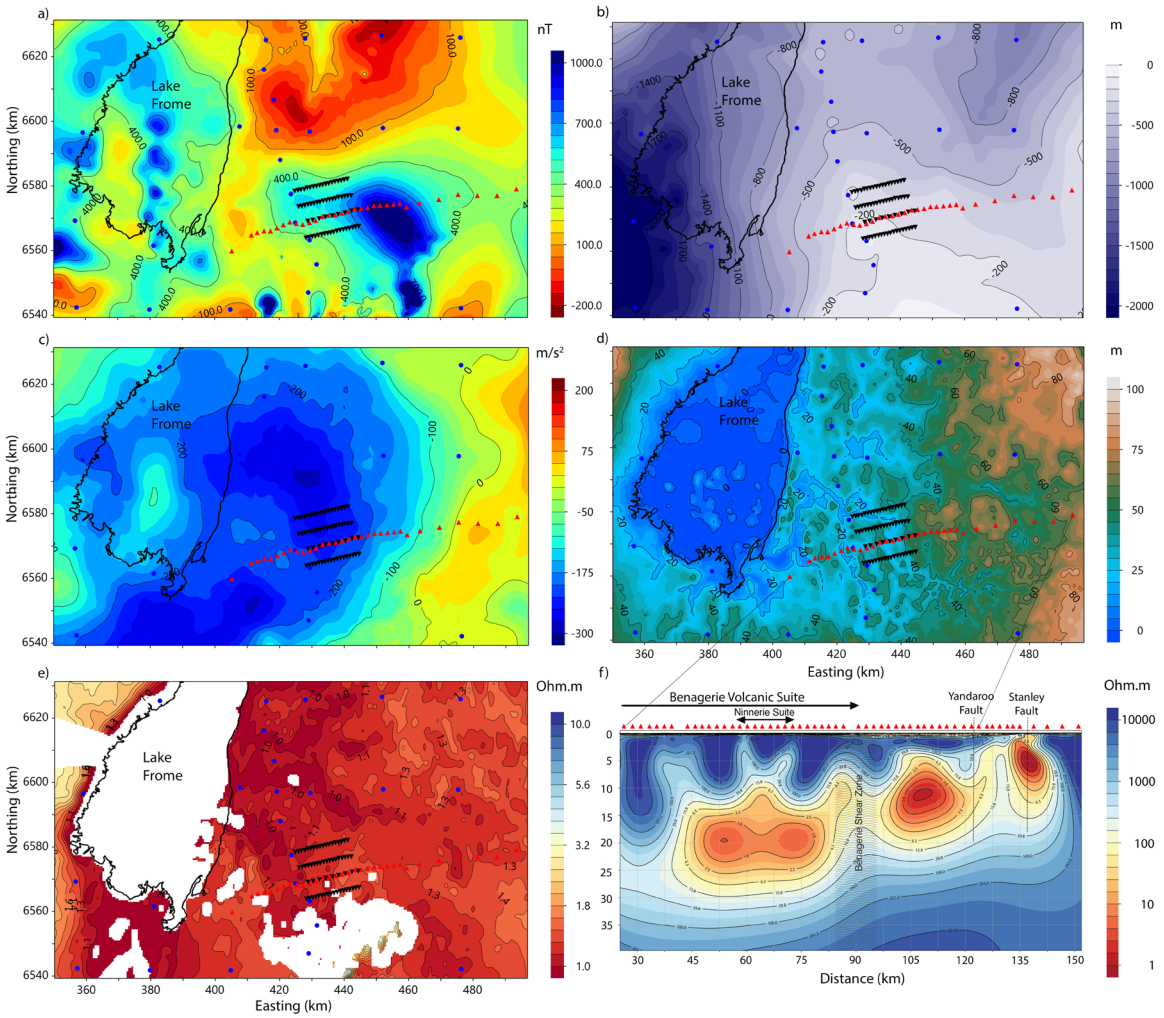

Figure 2: a) CCMT 2017 stations (red triangles) and 2021 Jupiter MT stations (black triangles) with regional Curnamona Cube MT stations as blue dots, overlain by gridded potential field magnetic dataset. b) Contour map of depth to basement in metres relative to sea level. c) Ground level gravity in m/s^2. d) Elevation map over the same area represented in metres above sea level. e) Aerial Electromagnetic (AEM) data averaged over the upper 100 m. f) 2-D cross section model to ~35km depth from CCMT_2017 transect, as per (Kay et al. 2021).

METHODS

MT Theory

The theory of the MT method was pioneered in the 1950's, using Maxwell's equations to provide information about the electrical resistivity vertical and lateral variations within the Earth's crust (Tikhonov 1950, Canigard 1953). It is classified as a natural source EM technique because it utilises the Earth's time-varying magnetic (**H**) and

electric (**E**) fields (Simpson and Bahr 2005). By simultaneously measuring variations in **E** and **H** fields at orthogonal angles on the surface of the earth, the impedance tensor (**Z**) can be derived. This relationship is shown in equation one, where x and y subscripts refer to orthogonal axes, usually aligned North and East.

$$\begin{pmatrix} E_x \\ E_y \end{pmatrix} = \begin{pmatrix} Z_{xx} & Z_{xy} \\ Z_{yx} & Z_{yy} \end{pmatrix} \begin{pmatrix} H_x \\ H_y \end{pmatrix} \quad (1)$$

Apparent resistivity (ρ_a) can be derived from the impedance tensor as a function of frequency, by the relationship described in equation two. Here μ_0 is the magnetic permeability of free space and ω is angular frequency, given $\omega = 2\pi f$ (Heinson et al. 2018b).

$$\rho_a = \frac{1}{\mu_0 \omega} |\boldsymbol{Z}|^2 \quad (2)$$

The exponential decay of electromagnetic fields as they attenuate through the Earth can be approximated as per equation three. This is referred to as the Skin Depth equation where T denotes the period of induction, given by the inverse of the frequency $\left(\frac{1}{f}\right)$. As such, the Skin Depth can vary from tens of metres to several hundred kilometres, depending on the period of the signal and the resistivity of the medium through which it travels.

$$\rho(T) \approx 500\sqrt{T\rho_a} \quad (3)$$

There are several assumptions which can be made based on whether the data is being modelled as a 1, 2, or 3-Dimensional Earth. Notably, conductivity varies only with depth for a 1-D model, hence the diagonal components of Z can be set as zero and the off-diagonal components are equal in value with opposite sign ($Z_{xx} = Z_{yy} = 0$ & $Z_{xy} = -Z_{yx}$). For a 2-D model, conductivity varies in depth as well as one horizontal

direction. Thus, the diagonal components of Z are equal and opposite in this case, while off-diagonal values are independent ($Z_{xx} = -Z_{yy}$ & $Z_{xy} \neq Z_{yx}$). Although to simplify, Z can be rotated in a purely 2-D structure to align along magnetic strike and again set the diagonals to zero.

The complex impedance tensor can be written in terms of real (**X**) and imaginary (**Y**) parts, per equation four (Heinson et al. 2018b). From this, the phase tensor can be defined by equation five which can be visualised as an ellipse with the major and minor axes representing the principal axes of tensor (Caldwell et al. 2004).

$$\boldsymbol{Z} = \boldsymbol{X} + \boldsymbol{Y}i \tag{4}$$

$$\phi = \boldsymbol{X}^{-1}\boldsymbol{Y} \tag{5}$$

The observed and regional phase tensor are identical as they are independent of the distortion tensor. As such, the phase tensor provides information about the dimensionality of the structures at any depth without being affected by distortion.

The skew angle (β), defined by equation 6, is a measure of the phase tensors rotation. In general, β is zero for the 2-D case and non-zero for the 3-D case. As such, a large value of the skew angle implies a 3-D regional conductivity structure (Caldwell et al. 2004).

$$\beta = \frac{1}{2}\tan^{-1}\left(\frac{\phi_{xy}+\phi_{yx}}{\phi_{xx}-\phi_{yy}}\right) \tag{6}$$

Survey

In an area approximately 25 km West of Lake Frome in South Australia, an array of four profiles containing 63 broadband MT sites were deployed, during May 2021. The profiles were 5km apart with 1km spacing between each site, as shown in figure one. Profiles A, B and D contained 18 sites, while profile C intersected a transect previously

collected with 2km spacings, so only contained 9 sites to infill to 1km spacing. Data was collected using AuScope Phoenix MTU-5C and Geoscience Australia Phoenix MTU-8A instruments. These were left out for 18-24 hours to collect signals within 0.01-10,000 Hz. All units were time-synchronised with onboard GPS and a remote reference site was run approximately 100km South of the array to correct for variation in the Magnetic field.

Prior to the survey, a calibration was performed on all receivers, electrodes, and magnetic coils. Similarly, the calibration process was repeated at the end of the survey to check for any damage to equipment, particularly magnetic coils after enduring vibrations throughout the deployment process. Additionally, a SD card was pre-programmed for each receiver to record two second intervals at 24,000 Hz, every 30 s and continuously at 150 Hz to obtain MT responses at 10,000 Hz and lower. Data was recorded on four channels, with two electric channels E_x and E_y, as well as two horizontal magnetic channels B_x and B_y, with no vertical magnetic field recorded. Two pairs of Borin Stelth-1 Ag-AgCl electrodes were buried 50m apart, oriented along magnetic N-S and E-W to measure the electrical potential difference in μV/m. Phoenix MTC-150 induction coils were also buried oriented N-S, E-W to record the frequency domain of B_x and B_y in ρT.

Time series data recorded to SD cards at each station was processed using Phoenix's EMpower geophysical software package. Calibration data was able to be applied using this program, before being converted to the frequency domain. Editing in cross-powers allowed time masking to be applied, removing interference in electric fields caused by

the helicopter take-off and landing. MT data from the survey were exported from EMpower as EDI files, which were then imported into the CGG Geotools program for modelling.

In conjunction with this project, a 25 km grid spaced array of 300 x 300 km over the Curnamona Province was completed to image the electrical resistivity to lithospheric depths. Some of these MT stations were included in 3-D modelling to provide constraints on edging effects.

RESULTS

Data quality

The quality of data collected for the Jupiter array was of a high standard, with minimal noise masking required. A major static shift correction was only required for one MT station (JD_10), where xy was shifted ~11Ωm and yx was shifted 1.5 Ωm. The skew angle for phase tensor data was evaluated along each profile and is presented within figure three. For all profiles, the skew angle boundary change occurs at a period of ~50 s. At longer periods, the value of beta is typically over 5^{o}, and thus beyond this phase, there start to become issues with modelling using anything other than 3D techniques. As such, the data can be modelled in 1-D and 2-D up to this period. Each profile also has a period of ~ 0.2 to ~15 s, where the phase tensors appear more ellipsoid. This suggests a larger difference between the maximum and minimum phase over this range. Some masking of data was required and is also visible in figure three, where phase tensor disks are missing. Notably, a large amount of data points from JA09,10, 11, JB04, 05, 16, 17 and JD14 were masked.

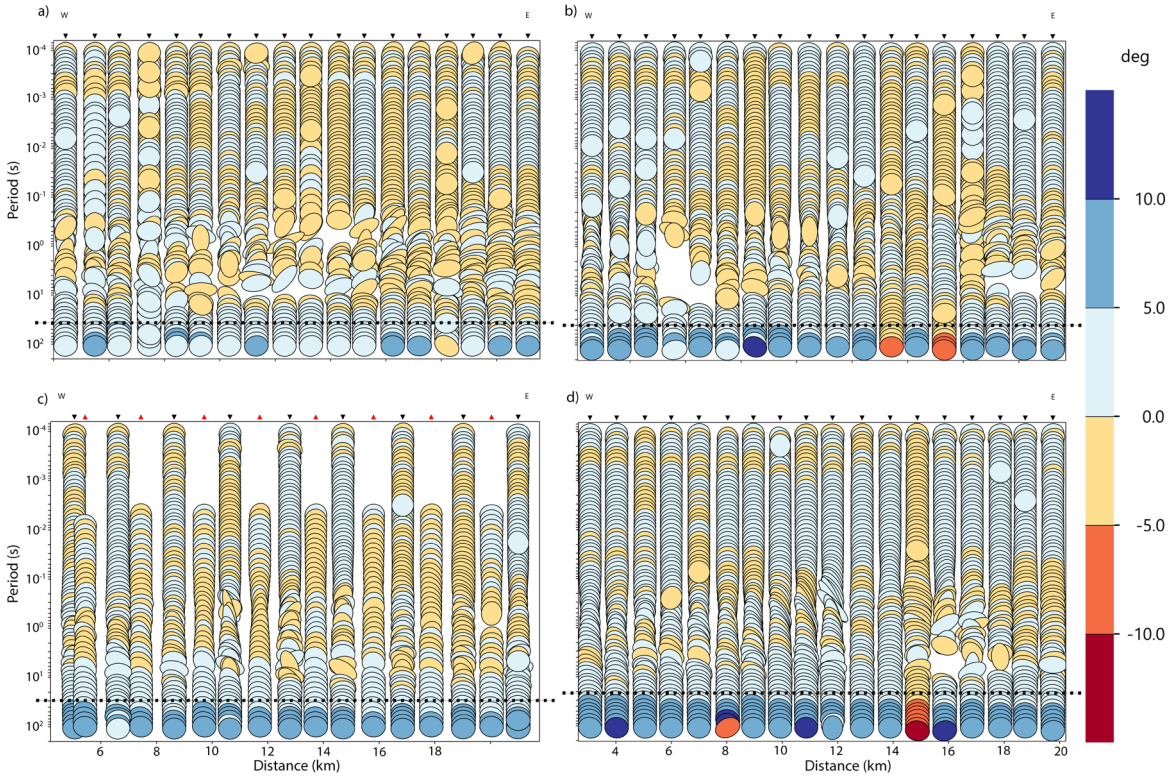

Figure 3: phase tensors skew (β) angle up to 100 seconds along a) profile A, b) profile B, c) profile C, d) profile D. Black triangles represent MT stations from 2021, while red triangles are from the 2017 CCMT transect. The black dashed line represents the point along each profile where the skew angle becomes >5°, and thus is considered to have 3D structure.

3-D model

A 3-D model was created using a mesh defined in the CCG Geotools software suite. This included an inner core mesh with cell sizes of 500 m with an outer mesh at 5 km, which extended 160 km E-W and 100 km N-S. Broadband MT sites from the Curnamona Cube project were included in the outer area as the Jupiter array itself is too small to define the scale expected of the regional geology. Each profile is 20 km in length and hence regional metamorphic and thermal processes of scale length greater than 20 km are not able to be imaged using this array alone. Parameters of the model are presented in appendix A.

By including the outer regional MT stations, this model aims to understand how the Jupiter array presents relative to more regional structures. As such, this model is a good representation of the broadly conductive and resistive regions, mapping out larger features. This is presented in figure four, with depth slices at 0.5, 2, 10 and 20 km. It shows at 500n m, the area within the array is considerably less conducting than surrounding areas. This correlates with a topographic high in the basement geology and may represent the depth at which there are no longer any sedimentary cover. At 2 km, the model suggests the array is largely resistive. At 10 km depth the array is still resistive, although there appears to be a large conductive region adjacent to the East. By 20 km dept, the entire array is conductive, with a region of 1 Ωm in the North-East corner. Notably, this model appears to be relatively homogenous in a lateral extent across the array. Also, structures appear to be focussed on the Jupiter array, indicating the meshing and irregularities in site spacing are dominating the responses.

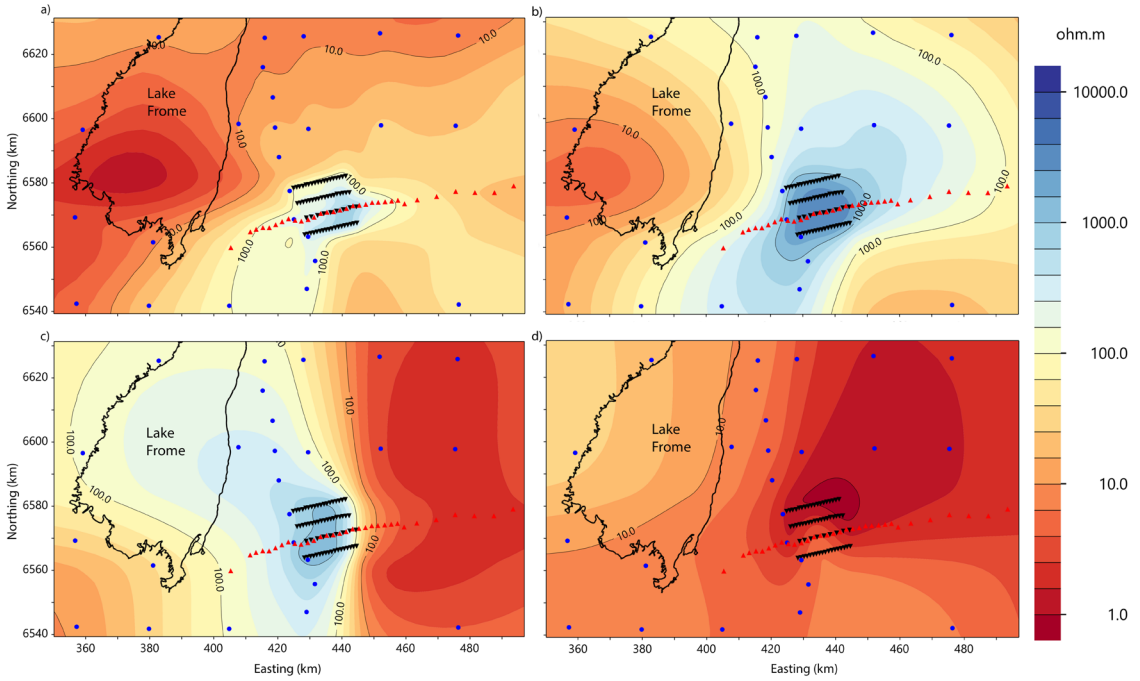

Figure 4: 3-D inversion model depth slice at a) 500m, b) 2km c) 10km, d) 20km. Note the black outline represents the extent of Lake Frome, red triangles are 2017 CCMT stations, black triangles

are Jupiter MT stations and blue circles are MT stations from the regional Curnamona Cube project.

2-Dimensional Regional Model

As established in figure three, the Jupiter data set is largely 1 and 2D, up to ~50 s. Moreover, the 3D model shows structures which are roughly 2D along Profile C. For this reason, a 2-D model was run including all sites from 2017 as well as the new Jupiter MT stations, modelled to 20 km depth. This model has a more consistently high density of sites in comparison to the 3-D model, with 1-2 km spacing for over 100 km. Consequently, this allows a better resolution in imaging electrical resistivity structures, at greater depth. This is presented in figure five, where geological information has been overlaid. See appendix B for details of model set up and fits of apparent resistivity and phase invariants.

Predictably, figure five agrees with the model presented in figure two f, as per (Kay et al. 2021). It shows two conductive bodies, with C1 of particular interest, buried beneath the Ninnerie Suite. Directly above this body, there are two gaps between the overlying resistive blocks (R1, R2, and R3), which continue up to the surface. These lower resistivity pathways labelled C3 and C4 are consistent with previous models (Kay et al. 2021, Kay 2017). The model presented in figure five shows the features C3 and C4 as less resistive than earlier models. Where previously C1 was 100 Ωm at 5km depth, this isosurface is shown at ~ 10 km in figure five.

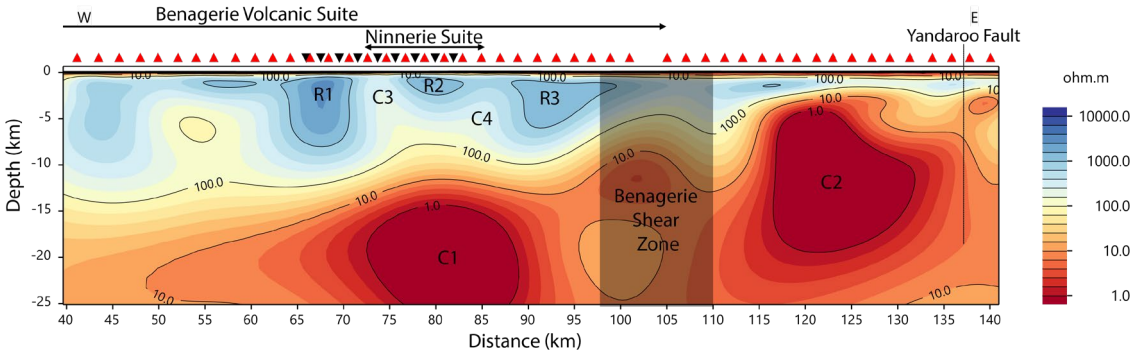

Figure 5: 2-D cross sectional model of Jupiter profile C (black triangles), extending 100km to include 2017 CC MT stations (red triangles). Conductive features C1 occurs at ~15-30km depth and C2 5-20km depth. Of particular interest are the regions which exist between resistive blocks labelled R1, R2 and R3.

2-Dimensional Jupiter Models

2-D cross sectional models across each of the four Jupiter profiles were generated across the bandwidth from 0.0002 to 50 s. Note these models included cells down to 100 km depth, however only the upper 12.5km are presented within figure six. This is because the deeper structures are more likely to be 3D. Furthermore, each profile is 20 km long and hence any features beyond 12.5 km depth cannot be accurately imaged. This is in comparison to the transect in figure five which is over 100 km in length.

Each model images a conductive upper surface, likely representative of the sedimentary cover sequences, over a resistive layer. For profile A, this layer extends across the entire length of the model. This model also presents a conductive body (1 Ωm) along the Eastern end at ~12 km depth. This feature labelled C1 also appears in profiles B and C, although it extends past the depth at which it cannot be accurately imaged.
Within profile B, there appears to be a zone of decreased resistivity below sites JB06-10. Profile C shows a complete break through the resistive layer from a conductor at depth through to the upper surface, this has been labelled C2 within figure six. It is the

only model where such a feature extends the entire distance from conductor to surface. This pathway at 5km depth is ~250 Ωm, bound between a resistive zone to the west (R1) and East (R2) of ~3981Ωm and ~2512 Ωm, respectively. Profile D also contains a region of decreased resistivity, however, does not drop below 1000 Ωm for the entire layer, similar to profile B.

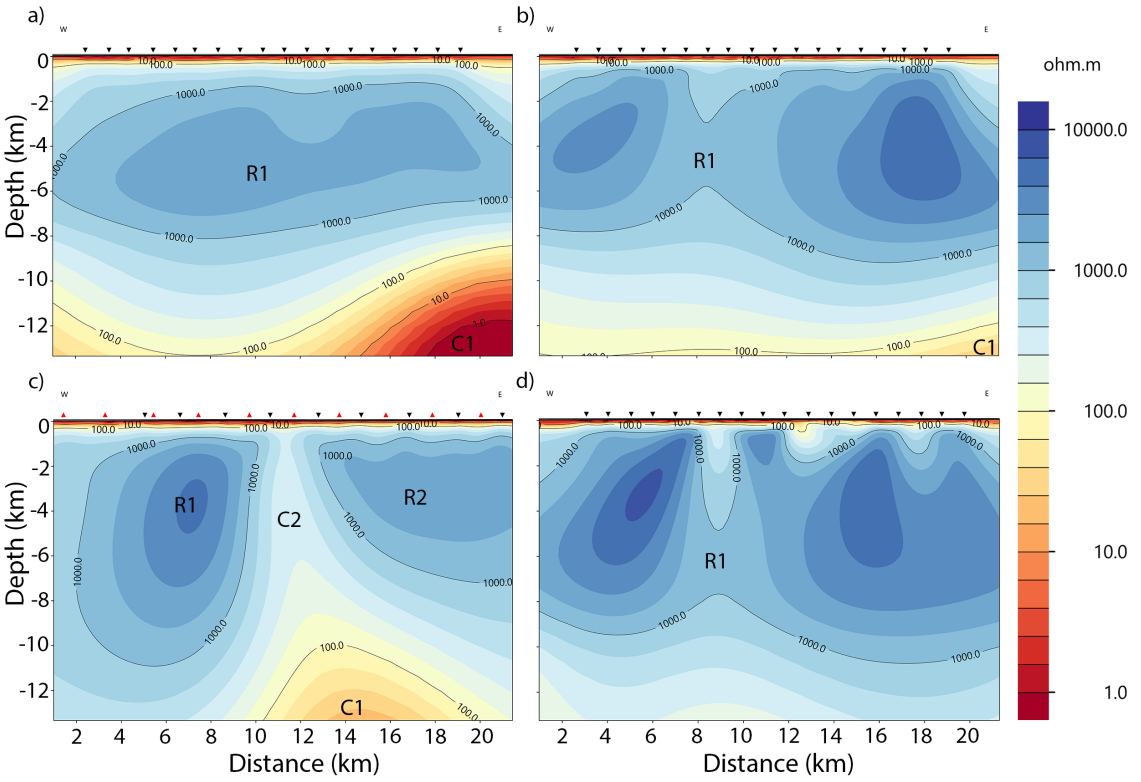

Figure 6: 2-dimensional cross sections for the upper 12.5 km along profiles a, b c & d. The same scale bar is used for all models, a conductive region C1 (<1Ωm) is imaged in profiles a, b, and c, but is absent in d. C2 represents a low resistivity pathway between resistive blocks R1 & R2.

1-D Batch inversions

As noted previously, the Jupiter array data is largely one and two dimensional up to ~50 s. However, it is not overtly distorted in a 3-D sense; it does not contain any phases out of quadrants or large changes across the array. Hence, a 1-D batch inversion was created to extract the information from each MT station as if the earth below was purely isotropic. This is presented in figure seven, where depth slices are taken at 0.5, 2, 10 and

20 km depth. See appendix D for parameterisation of model and fits of normalised phase and apparent resistivity invariants.

Figure seven a highlights a circular conductive region over MT stations CC15 and JC04, with an increasingly resistive region over the S-E corner of the array. The model then generally becomes more resistive with increasing depth, with the entire array contained within 398-1584.9 Ωm at 2 km. Notably a slightly less resistive area around the MT sites CC 15 and JC 04, also exists at this depth. At 10 km depth, this region is significantly less resistive than the surrounding areas with concentric isosurfaces surrounds the sites CC15 and JC04. At 20 km depth the entire array is generally conductive, with the majority less than 10 Ωm and a portion in the South-Eastern corner ~40-10 Ωm. This is in comparison to the 3D model of the same depth, which presents a slightly more conductive area and shifts the less conductive region towards the centre of profile D.

The less resistive region which exists broadly within all depth slices presented in figure seven, has been labelled C1 to represent a pathway from a conductive region at depth to the upper surface. Another notable feature of the model is that the profile A is generally more conductive than the other profiles, with each become increasingly resistive further South along the array. In summary, this 1-D model presents a conductive upper crust above a resistive region from ~1 – 10 km. This layer has an electrical resistivity low around the centre of profile C and continues at depth to a conductive layer at 20 km depth.

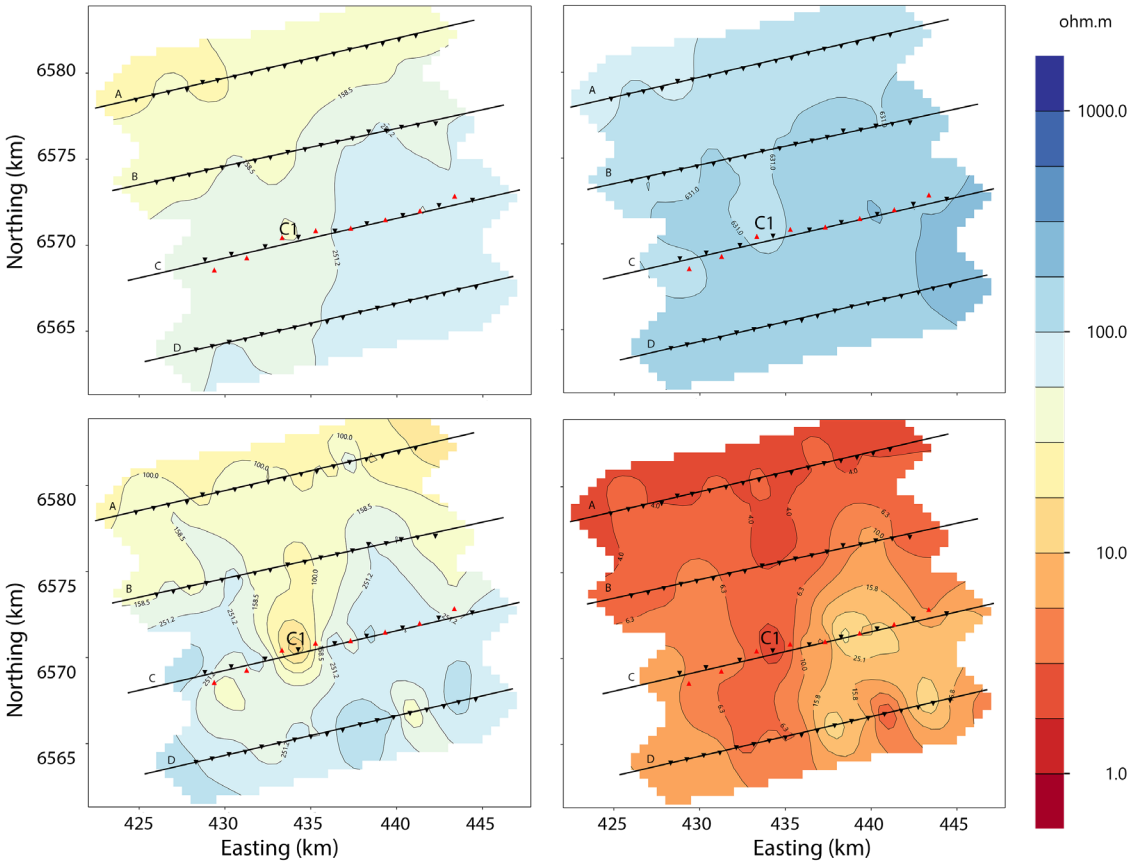

Figure 7: 1-D inversion of MT data depth slices at a) 500 m, b) 2 km, c) 10 km and d) 20 km. C1 has been labelled to highlight the persistent conductive structure in between two resistive (R1 & R2) blocks. Easting and Northing are given in km are using WGS 84, UTM Zone 54S.

DISCUSSION

Overall, the models presented in the results section concur to a large degree despite using various data points as well as different parameters, resolutions, and bandwidths. Specifically, the 1 and 2-D models agree on the general electrical resistivity structure of the array including a low-resistive pathway surrounding sites CC15 and JC04. Comparatively, the 3-D model does not present any low-resistivity pathways through the resistive region. This result implies that either the 1 and 2-D models are incorrect or that the 3-D model is wrong. Given that the 3D models include the entirety of the impedance tensor, it should present the structural feature in better resolution (Avdeeva et al. 2015). However, the inherent smoothing required for 3-D inversions, removes any

weak structures. It has been observed that 2D inversions produce stronger resistivity contrasts than 3-D. This is due to the distribution of the conductance into the third dimension, hence smoothing out the model (Robertson and Thiel 2019). As such, the 3-D result is not necessarily wrong, it just doesn't present the detail seen in other models. Broadly comparing figures three and seven, it is evident that to a large degree the 1 and 3-D models do concur. They similarly present a conductive upper surface, a resistive layer from 0.5 – 10 km, and a conductive layer at 20 km depth.

These models lack independent constraints as even though they draw upon different parts, they are mostly built using the same dataset. Hence, if for any reason there is bias within the data, all the models will also be biased. Consequently, independent data sources are extremely useful in verifying the validity of results. However, the Curnamona is relatively under-explored, with minimal outcrop present (Dentith et al. 2003). Paucity of drill hole data over the area means there is a lack of geochemical data available to corroborate at present. As one means of comparison, the outputs from 1-D batch inversion model were compared to AEM data, available online, over the same area. Specifically, the AEM depth slice from 80-90 m was compared to the 1-D model at 80 m. The results show consistency between the two models at this depth, with very similar shaped electrical resistivity structures, as presented in figure eight.

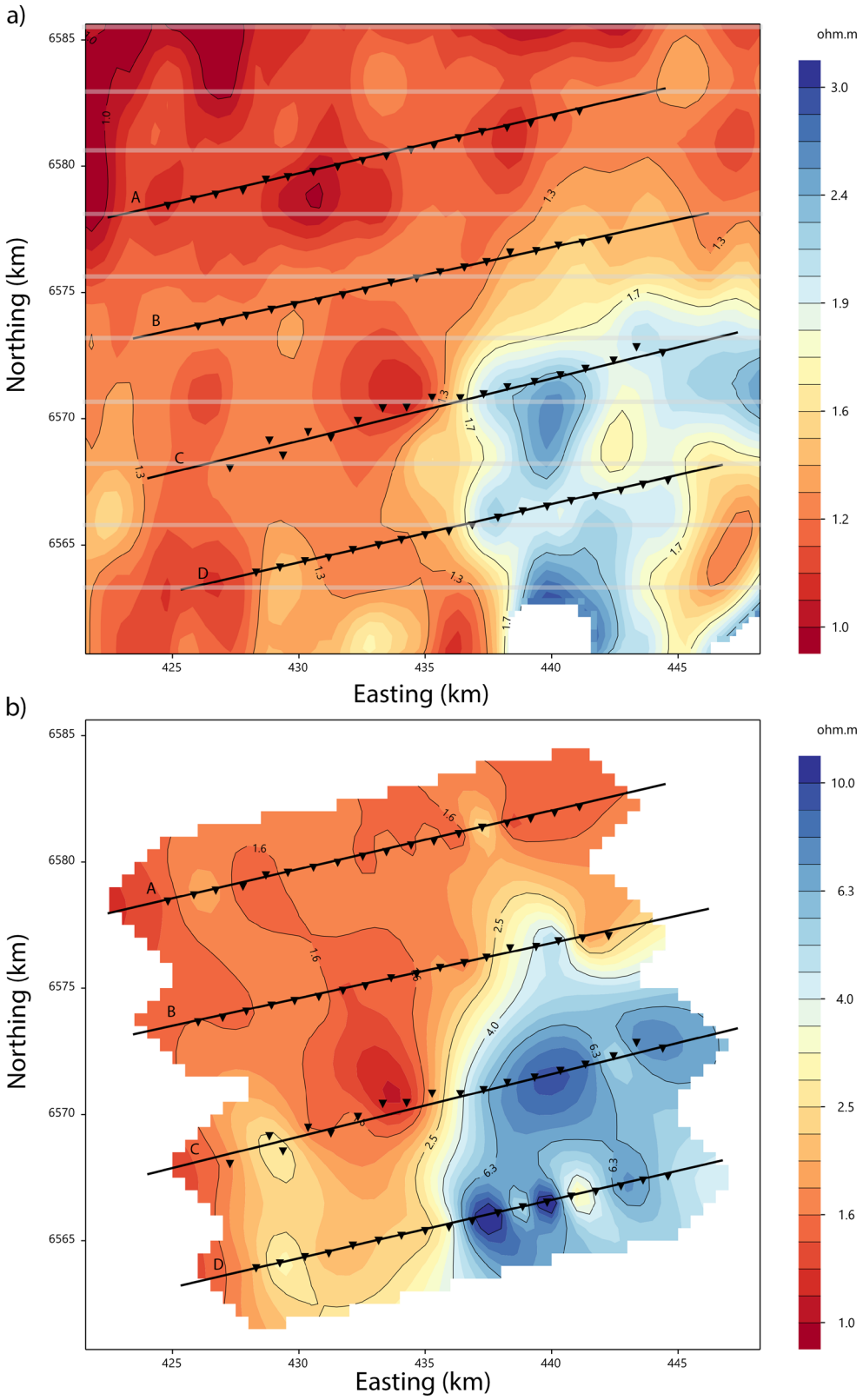

Figure 8: a) AEM depth slice from 80-90 m. Note the MT stations and profiles are only for reference locations and the data is independent of these sites. The grey horizontal lines present the flight path of 2.5 km spacing. b) 1-D MT batch inversion at 80m, showing a similar resistive region over the South-Eastern portion of the array as well as conductive anomaly along profile C.

Although the colour scales within this figure are not the same, they are of the same order of magnitude. Overall, the contour lines trace out a very similar pattern over the array for both models, with a resistive region in the South-Eastern corner. These independent results provide confidence in the validity of both models down to this depth.

This correlation between independent models is significant as it shows the electrical resistivity structures of the upper 100 m have been accurately imaged. As the electrical signals from the structures at depth must pass through this region to the receiver at the surface, it provides confidence that they are not being distorted here. It should be noted, however that AEM and MT data are susceptible to similar errors, due to the way that the area which the signal is drawn from increases with depth. As such, the area over which the signal is being drawn from at greater depth increases and may not actually represent the earth directly below the signal receiver (Palacky 1993).

As highlighted in results, all models show a generally conductive upper crust to ~100 – 300 m depth, although obviously there is variation in this depth across the array. This boundary could be explained as the depth to basement as generally sediments have a high porosity and can contain pore fluids, resulting in conducting properties (Robertson and Thiel 2019). This depth does coincide with the depth of Cenozoic cover over the area as mapped by (Fabris et al. 2010). This further promotes a high degree of accuracy within the uppermost layers of the models.

To quantify the uncertainty of the electrical resistivity structures imaged in the 2-D model over Jupiter profile C, a bootstrap model was run. This resampling technique provides multiple solutions which are then statistically analysed to determine the variability between the different solutions (Schnaidt and Heinson 2015). The original dataset was repeatedly resampled with 10 randomly selected MT stations removed each time. In total, 16 subsets of 20 stations were modelled before being exported as text files and statistical analysis was calculated using a MATLAB script. The outputted logarithmic mean model is shown in figure nine. Of particular interest is the pathway (C1), between the two resistors (R1 and R2). This feature is not as significant as in the original 2-D model of profile C; here it is of the range 631-1000 Ωm. Despite these values clearly not being conductive, there is a defined structural feature where the resistivity is lower than R1 and R2. Hence it can be inferred that this feature of lower resistivity is statistically verified, within the model.

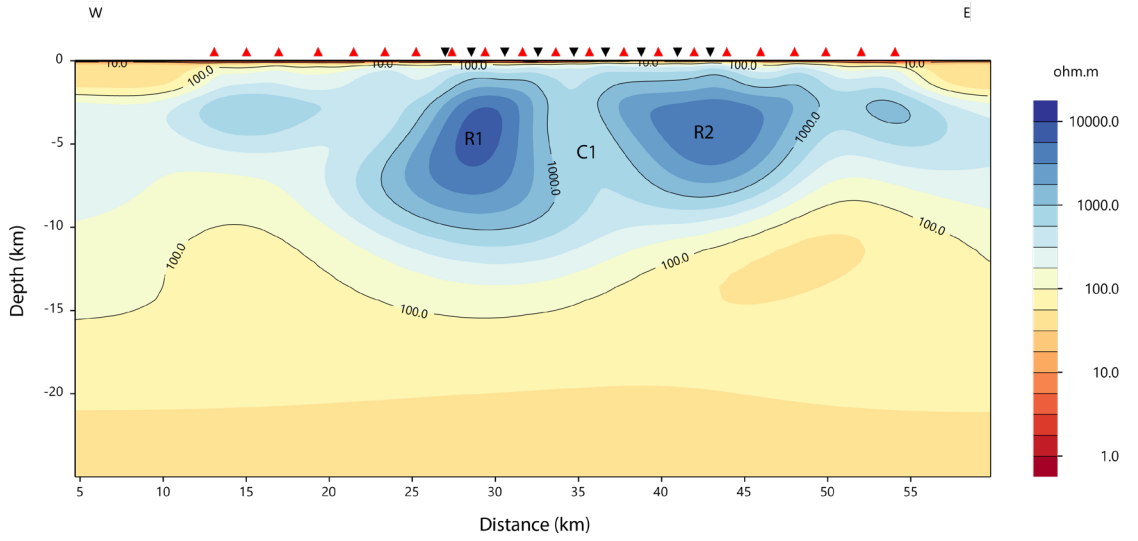

Figure 9: Bootstrap model of the logarithmic mean of profile C, including CCMT_2017 stations 06-26 and Jupiter C1-9. It shows a relatively conductive pathway from the upper crust to a depth of ~15km. This provides confidence in the model presented in figure 3, as this feature, although weak is statistically present in the data. Notably, the conductive region at ~15km depth also appears to be much weaker and ~10Ωm instead of 1 Ωm presented in figure 6c.

A similar bootstrap model of the standard deviation normalised by the mean value is presented in figure ten. This highlights the areas of most confidence at zero and the least confident at 100. The most certain regions appear to be lateral structures at ~15 km depth, labelled C2. Notably, this aligns approximately with the point in the model at which it turns from largely conductive to variably resistive. Similarly, other conductive regions including the upper surface and the central pathway labelled C1 are relatively confident structures. Evidently this test appears to correlate statistical confidence to those structures of higher conductivity within the models. Moreover, the more resistive structures have a low confidence, with R2 the most variable feature.

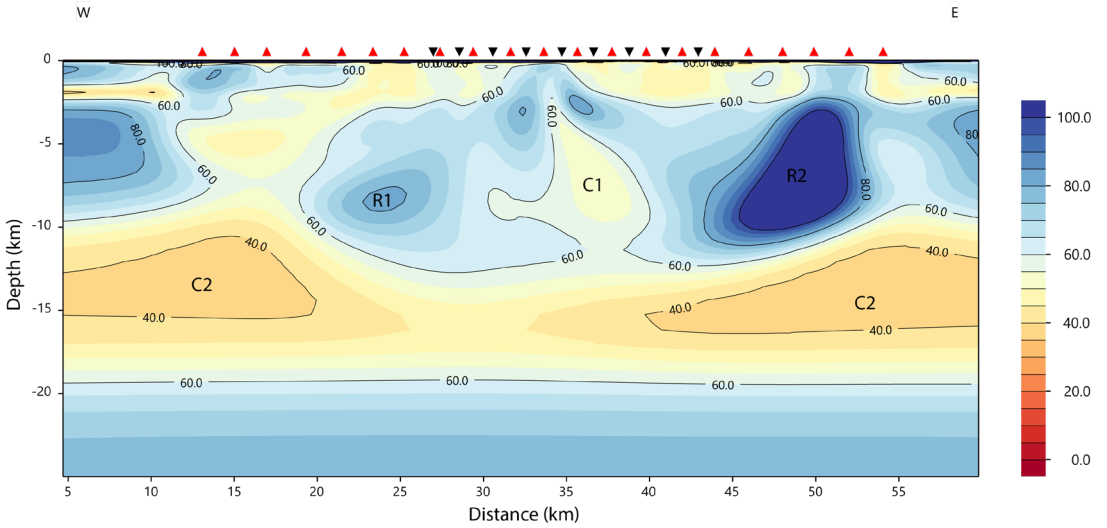

Figure 10: bootstrap model of the percentage deviation for each cell within the model. Zero represents no doubt in the structure, while 100 indicates no confidence that the feature exists within the electrical resistivity structure.

The models shown in figures nine and ten present the total 30 stations included in the bootstrapping. However, for each subset one third of the sites were removed, leaving only 20 MT stations per model. Given this, if the imaging of a structure was solely dependent on one station, it would be expected that one third of the models would not present it. Consequently, a large variance should occur over that region, as it would be

one of the least well resolved points. Evidenced by figure ten, the percentage deviation for C1 is smaller than other parts of the model, showing that it has a low variance. This provides a strong argument that this structure does exist within the Earth.

As with any MT modelling, there are issues with non-uniqueness where a model may fit the data statistically, despite being nothing like reality. Despite this, these models provide a statistical understanding of the robustness of the feature. Unfortunately, this bootstrap approach can only effectively be done for 2-D models as it is too computationally exhaustive to run 16 subset models in 3-D. In theory, a 1-D model could be completed, by re-gridding the 80 MT stations, into subsets. However, this will not change the modelling information, merely adjusting the gridding between points. Consequently, it is not a particularly useful insight, and a 1-D bootstrap test was not performed.

To verify the role of this feature in terms of defining a mineral system footprint, comparison to other data sets is critical. Regional geophysical datasets, including gravity and magnetic potential field data, are available and have been presented within figure two. Ultimately, there is a lacking in terms of other geophysical or geochemical data which the models could be compared to within the Curnamona Province. As a further means of evaluation, results were compared to other known mineral system footprints. For this, a dataset from the Gawler Craton, comprising a MT transect across Olympic Dam and other major mines of the Stuart Shelf, was utilised. This area shares many geological similarities including age and relative spatial proximity to the Curnamona Province. Furthermore, it underwent a similar style of magmatism with the

Hiltaba Suite Granites reminiscent of the Benagerie Ridge flood igneous plateaus within the Curnamona Province (Wade et al. 2012).

A 2-D model of MT data from the Stuart Shelf is imaged to the same linear extent, with the same colour scale for resistivity as the regional 2-D model. This comparison is presented in figure 11. The Stuart Shelf survey, completed in conjunction with a seismic program, identified a region of low resistivity (<10 Ωm) over 50 km wide at 15km depth. As identified by Heinson et al (2018), this conductive anomaly coincides with the brittle-ductile transition, above which three low resistivity zones extend up to the surface (Heinson et al. 2018b). The conductive anomaly is labelled as C1, with the three pathways C2, C3 and C4, markedly branching upwards to known mineral deposits at Wirrda Well, Olympic Dam, and Vulcan. These pathways sit between resistive blocks labelled R1, R2, and R3. Significantly, the pathway of lowest resistance (100 Ωm) extends up to Olympic Dam; the largest known deposit of uranium and fourth largest copper deposit world-wide (Ehrig et al. 2012).

Figure 11 b presents similar pathways to those of 11a, although the conductor at depth (C1) is an order of magnitude lower resistivity (1 Ωm compared to 10 Ωm). Additionally, the major pathway (C3) within figure 11a is of considerably lower resistivity than C3 of 11b. In terms of resistivity values, the pathway extending up to the Vulcan Deposit (C4) within 11a is more analogous to C3 of the Jupiter model. Overall, there are many similarities in the electrical resistivity structure of these two models. While the electrical resistivities of rocks and other common Earth materials span 14 orders of magnitude, some materials vary greatly depending on the setting. Graphite

film in rock matrix has produced resistivity values of 10^{-3} – 10^{5} in laboratory testing, depending on connectivity (Simpson and Bahr 2005). Hence these variations in electrical resistivity values may simply be explained by connectivity of graphite film.

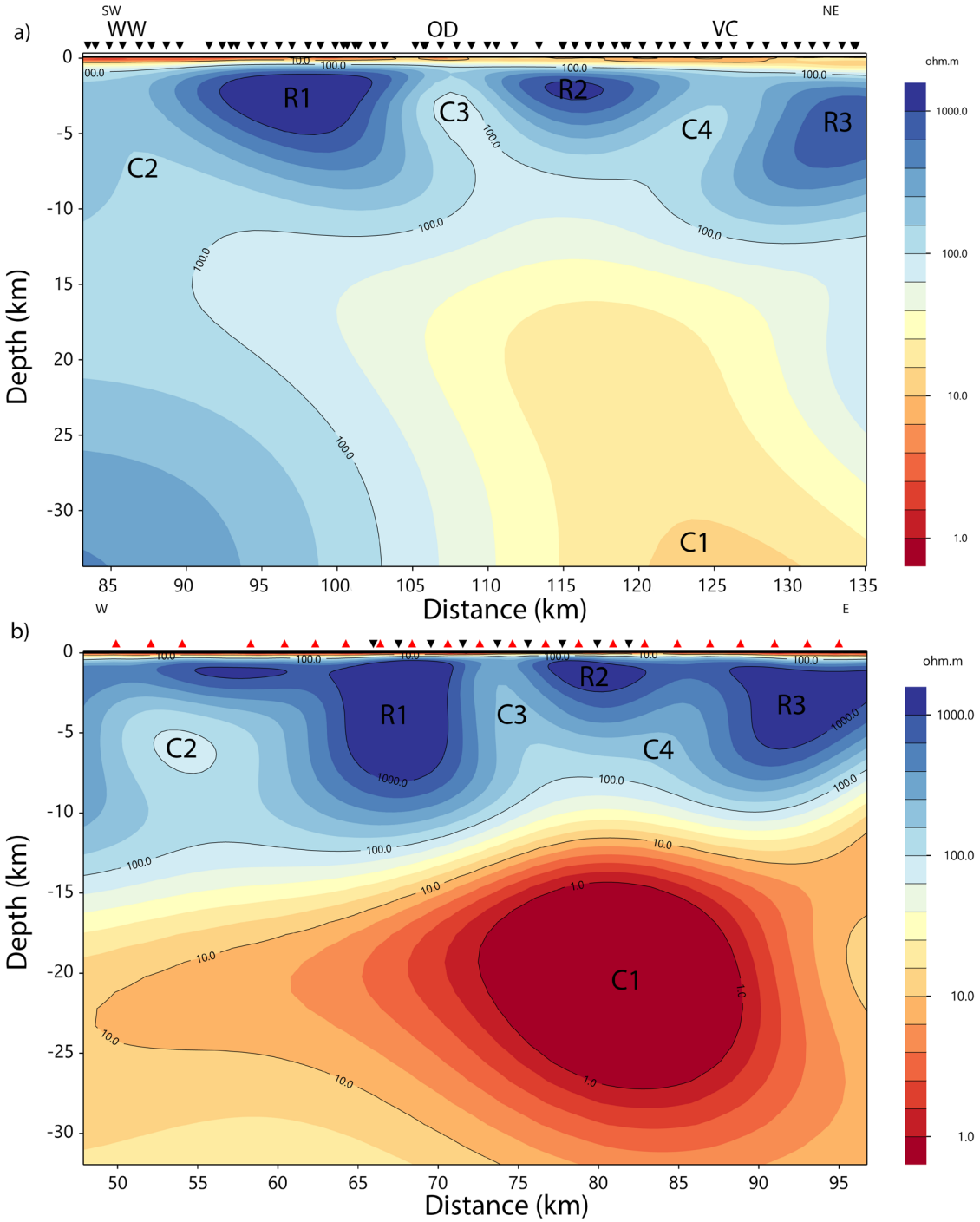

Figure 11: a) 2-D resistivity model of the Gawler Craton to 30km depth. WW, OD, and VC represent major mineral deposits Wirrida Well, Olympic Dam, and Vulcan. b) regional 2-D

resistivity model over the Curnamona Province. Note this is the same model as in figure 5 but focusses on a smaller linear scale and reduced colour scale.

As another means of comparing the results to those of known mineral systems, a 1-D inversion model was created, using MT data surrounding the Carrapateena mine. This IOCG deposit, also within the Gawler Craton has been demonstrated as having similar properties to Olympic Dam, albeit on a smaller scale (Vella and Emerson 2009). The 1-D Carrapateena model is shown in comparison to the Jupiter array within figure 12. It presents similarities in the electrical resistivity structures of the two models at 5 and 10 km depth.

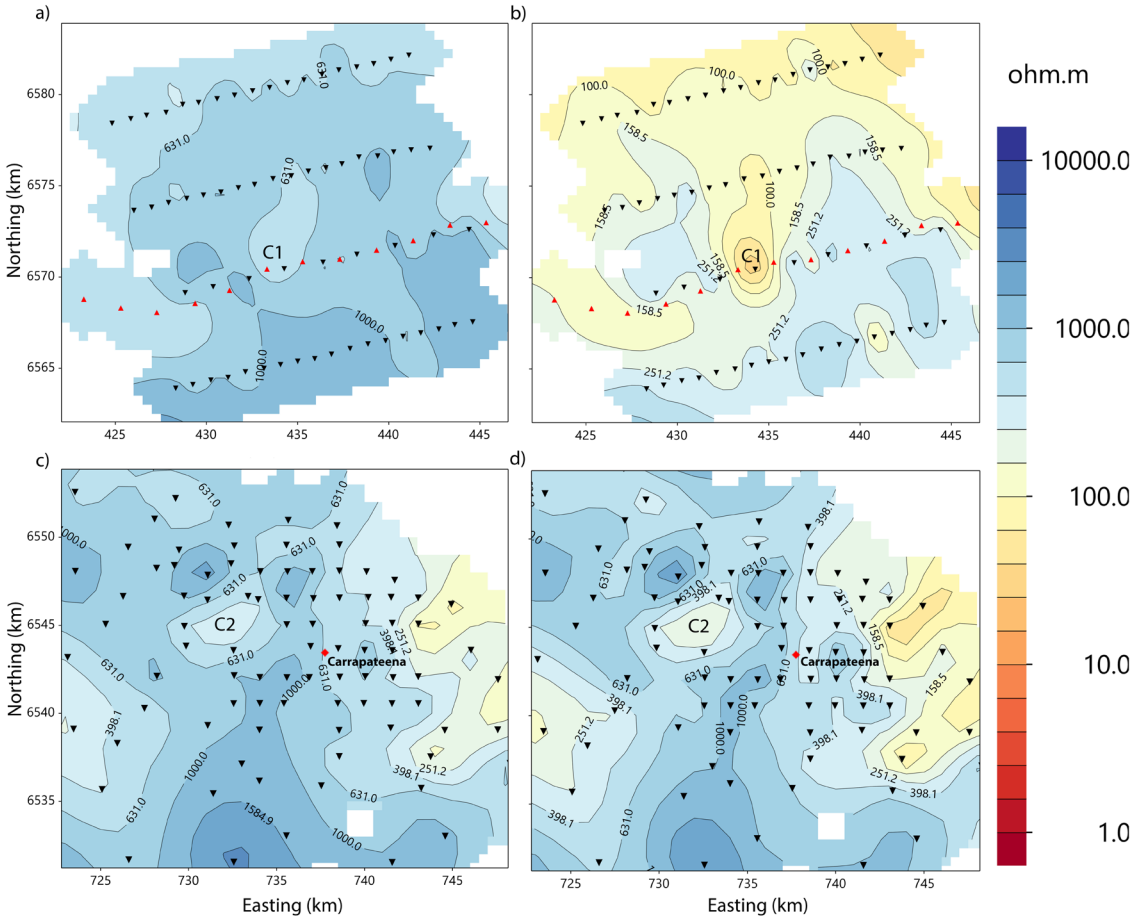

Figure 12: a) 1D batch inversion models of Jupiter site at 5 km depth. b) depth slice at 10 km. c) Separate 1D inversion surrounding Carrapateena IOCG mine (red diamond), at 5 km depth. d) depth slice at 10 km. Both models show similarities with a sub-circular feature surrounded by comparatively resistive material. Notably, Carrapateena does not sit on top of this structure, but exists ~5Km to the S-E.

Evident in figure 12b and d, the features labelled C1and C2 both appear as concentric isosurfaces flanked by resistive regions, although C1 is of the range 40 – 25 Ωm, and C2, 100 – 63 Ωm. While C1 appears to be of higher conductivity at 10 km, C2 appears to be a more consistently conductive feature, with a higher conductivity at 5 km. This is shown in figure 12 a and c where C1 is 630 – 340 Ωm, compared to 340 – 250 Ωm for C2. An interesting feature of the 1-D model over Carrapateena is that the IOCG deposit does not intersect C2 but exists approximately 5 km to the South-East. Contrastingly, the low-resistivity features presented in figure 11a appear to align directly underneath each deposit. Above the depths imaged within figure 12, the feature C2 remains in the same geographical location, up to ~1.3 km depth. This may represent a more 3-D pathway than the one imaged at the Jupiter array as C1 is clearly defined up to 500m depth, as per figure seven.

The electrical resistivity models over the Jupiter array in 1 and 2-D bear a resemblance to that beneath major mineral deposits within the Gawler Craton, as evidenced by figures 11 and 12. Despite the structural similarities, there are slight variations in resistivity values, often within the same order of magnitude. There are several factors which influence the perceived resistivity of the Earth including porosity, permeability, fluid saturation, pore fluid salinity and clay content (Nabighian M and Corbett J 1987). These play a particularly large role in the conductive characteristics of sedimentary cover sequences. This is evident in both the Curnamona Province and the Gawler Craton as models from both domains consistently feature a conductive upper sequence. This is a significant result as an informed understanding of depth to basement is crucial to defining the mineral system (Roach et al. 2018).

This is particularly relevant within South-Eastern Australia as the Olympic Dam deposit lies beneath 300 m of sedimentary cover (Heinson et al. 2018a), with the areas surrounding also covered by hundreds of metres of barren post-mineralisation cover (Krneta et al. 2017). Similarly, Carrapateena lies under 470 m of moderately conductive sediments of the Stuart Shelf (Vella and Emerson 2009). This is evident in the 1-D Carrapateena model, which presents a conductive layer (<60 Ωm) to ~500 m. In comparison, the Jupiter 1-D model only presents these conductivities for the upper 200 m. Note that there is a topographic high over the Jupiter array as per figure two b, with depth of Cenozoic cover at -100 to -400 m below sea level, over the array. This implies the depth to cover over the Jupiter anomaly is less than that above IOCG deposits of the Gawler Craton.

Another factor which affects the electrical resistivity, particularly around a copper deposit is the weight percent and interconnectivity of sulphides. Similar to graphite, sulphides are most conductive when connected in continuous veins, however, can appear resistive when disseminated (Jones et al. 1997). Although, at the scales imaged here, it is not likely that the structures seen are the result of a high sulphide concentration. The properties of the conductive anomalies (C1) within figure 11; 25 Ωm at 20 km in the Gawler Craton and 2 Ωm at ~23 km in the Curnamona, do not fit those which can be explained by sulphides (Yang 2011). This is important to the mineral system approach to exploration as these conductive zones may not image sulphides but the pathways of past fluid processes. This has implications for exploration targeting within Southern Australia as well as globally (Skirrow et al. 2018).

Imaging of lithospheric architecture and understanding of tectonic setting provide a robust framework for interpreting the spatial controls of IOCG as well as other magma derived deposits (Skirrow et al. 2018). Hence, by first looking at regional scale to determine the tectonic setting and understand the whole system, exploration targets can be re-defined (McCuaig and Hronsky 2014). Three common features are required for the genesis of an Au-Cu deposit; a mantle source region containing the elements, trans-lithospheric faulting, and a tectonic, potentially thermal trigger (Griffin et al. 2013).

Within the Jupiter array, there is evidence of two of these three factors. The presence of the Benagerie Volcanic Suite indicates a tectono-thermal event, with far-field subduction zone as a likely mechanical driver (Wade 2011, Wade et al. 2012). Additionally, the deeply rooted Benagerie Shear Zone provides a lithospheric-scale structural system (Williams and Betts 2009). The low electrical resistivity zones imaged here may provide a map of the pathways through which metals migrate from depth to the upper crust. However, this interpretation does assume that the magma source contains economic minerals at the beginning.

Similarly, these processes have occurred across geological time, with several periods of super-continental accretion and break-up over the history of the Earth (Griffin et al. 2013). The extent to which a craton may be able to retain an original signature or how it is subsequently deformed by such events is still relatively unknown. As such, it is possible that results imaged here may represent a mineral system which once existed but has not been preserved over time.

CONCLUSIONS

A new broadband (10^4 to 0.01 Hz) MT array comprised of four profiles of 1 km site spacing and 5 km line spacing was collected to build upon previous models of electrical resistivity structure within the Curnamona Province. This developed a better understanding of the dimensionality as well as increasing resolution of geophysical signatures. There is strong evidence for a low-resistivity pathway from a conductive anomaly at ~20km depth, to the upper crust. This is bound between two highly resistive blocks and is pervasively imaged at different scales in 1-D and 2-D inversion models. This structural feature has been robustly verified using bootstrap methods in 2-D. Modelling in 3-D agrees largely with the electrical resistivity structure of the Earth over the Jupiter array; however, it does not image the low-resistivity pathway due to inherent smoothing between sites. This conductive pathway may be representative of weakness within the rheology as it bears resemblance to the mineral system footprints beneath IOCG style deposits within the Gawler Craton. Further investigations including seismic surveys, drilling programs, and geochemical analysis is required to better constrain the role of these low resistivity pathways in terms of defining a mineral system.

ACKNOWLEDGMENTS

I acknowledge the Kaurna people as the traditional owners of the land on which Adelaide University North Terrace campus is built. I acknowledge the Malyangaba people as traditional owners of the land in which field surveys took place. I recognize both the Kaurna and Malyangaba people as custodians of these lands, and that their cultural and heritage beliefs, and spiritual relationships with Country, are still important to their people today.

I would like to thank my supervisor, Graham Heinson, whose guidance, enthusiasm and knowledge of the MT theory was invaluable. Thanks also to my co-supervisors Kate Robertson and Stephan Theil. Thank you to Geoscience Australia for datasets available online, AuScope for instrumentation, the Geological Survey of South Australia and Havilah Resources for funding provided to this project as part of the Accelerated Discovery Initiative from the Department of Energy and Mining. Thanks to Ben Kay for

organizing logistics of field work and general support both in the field and with troubleshooting data processing. Thanks to Tim Anderson and Erin from Helifarm for field logistics. Finally, thank you to Goran Boran for helping to teachings in the field and Yi He for coming along on this learning journey with me.

REFERENCES

ARMISTEAD S. E.*, et al.* 2018 Cu-Au mineralisation in the Curnamona Province, South Australia: A hybrid stratiform genetic model for Mesoproterozoic IOCG systems in Australia., *Ore Geology Reviews,* vol. 94, pp. 104-117.

AVDEEVA A.*, et al.* 2015 Three-dimensional inversion of magnetotelluric impedance tensor data and full distortion matrix, *Geophysical Journal International,* vol. 202, no. 1, pp. 464-481.

BOERNER D. E., KURTZ R. D. & CRAVEN J. A. 1996 Electrical conductivity and Paleo-Proterozoic foredeeps, *Journal of Geophysical Research: Solid Earth,* vol. 101, no. B6, pp. 13775-13791.

CALDWELL T. G., BIBBY H. M. & BROWN C. 2004 The magnetotelluric phase tensor, *Geophysical Journal International,* vol. 158, no. 2, pp. 457-469.

CANIGARD L. 1953 Basic theory of the magnetotelluric method of geophysical prospecting, *Geophysics,* vol. 15, pp. 193-204.

CHAMALAUN F. H. 1985 Geomagnetic deep sounding experiment in the central Flinders Ranges of South Australia, *Physics of the Earth and Planetary Interiors,* vol. 37, no. 2, pp. 174–182.

CONOR C. H. H. & PREISS W. V. 2008 Understanding the 1720-1640 Ma Palaeoproterozoic Willyama Supergroup, Curnamona Province, Southeastern Australia: Implications for tectonics, basin evolution and ore genesis, *Precambrian Research,* vol. 320, pp. 403-423.

DENTITH M., COWAN D. R. & HAWKE P. 2003 Geophysical characteristics of some Proterozoic base-metal deposits in the Curnamona province of South Australia, *ASEG Extended Abstracts,* vol. 2003, p. 101.

EHRIG K.*, et al.* 2012 Geology and Mineralogical Zonation of the Olympic Dam Iron Oxide Cu-U-Au-Ag Deposit, South Australia. Geology and Genesis of Major Copper Deposits and Districts of the World: A Tribute to Richard H. Sillitoe*.* pp. 0. Society of Economic Geologists.

FABRIS A., GOUTHAS G. & FAIRCLOUGH M. 2010 The new 3D sedimentary basin model of the Curnamona Province : geological overview and exploration implications, *MESA Journal,* vol. 58, pp. 16-24.

GOUGH D. I., LILLEY F. E. M. & MCELHINNY M. W. 1972 A Polarization-sensitive Magnetic Variation Anomaly in South Australia., *Nature Physical Science,* vol. 239, pp. 88-91.

GRIFFIN W. L., BEGG G. C. & Y. O. R. S. 2013 Continental-root control on the genesis of magmatic ore deposits, *Nature Geoscience,* vol. 6, pp. 905-910.

HEINSON G.*, et al.* 2018a The crustal geophysical signature of a world-class magmatic mineral system, *Scientific Reports,* vol. 8, no. 1.

HEINSON G.*, et al.* 2018b The crustal geophysical signature of a world-class magmatic mineral system, *Scientific Reports,* vol. 8 Suppl., no. 1.

JIANG W.*, et al.* 2019 Mapping Deep Electrical Conductivity Structure in the Mount Isa region, Northern Australia: Implications for Mineral Prospectivity, *Journal of Geophysical Research: Solid Earth,* vol. 124, no. 11, pp. 10655–10671.

JONES A., KATSUBE T. & SCHWANN P. 1997 The Longest Conductivity Anomaly in the World Explained: Sulphides in Fold Hinges Causing Very High Electrical Anisotropy, *Journal of Geomagnetism and Geoelectricity,* vol. 49, pp. 1619-1629.

KAY B. 2017 Testing the UNCOVER paradigm: Crustal fluid pathways in the Curnamona Province. Physical Sciences*.* pp. 30. Adelaide: University of Adelaide.

KAY B., HEINSON G. & ROBERTSON K. 2021 Crustal magnetotelluric imaging of a Paleoproterozoic graphitic suture zone, Curnamona Province, Australia. Gondwana Research (Unpublished)*.* pp. 1-28.

KRNETA S.*, et al.* 2017 The Wirrda Well and Acropolis prospects, Gawler Craton, South Australia: Insights into evolving fluid conditions through apatite chemistry, *Journal of Geochemical Exploration,* vol. 181, pp. 276-291.

LEYH W. R. & CONOR C. H. H. 2000 Stratigraphically controlled metallogenic zonation associated with the regional redox boundary of the Willyama Supergroup – economic implications for the southern Curnamona Province., *MESA Journal,* vol. 16, pp. 39–47.

MCCUAIG T. C. & HRONSKY J. 2014 The Mineral System Concept: The Key to Exploration Targeting, *Society of Economic Geologists Special Publication,* vol. 18, pp. 153-175.

MILLIGAN P. R. & LILLEY F. 2010 Magnetotelluric results along the N-S Curnamona seismic traverse to the east of Lake Frome, South Australia, *ASEG Extended Abstracts,* vol. 1, pp. 1-4.

MYERS J. S., SHAW R. D. & TYLER I. M. 1996 Tectonic evolution of Proterozoic Australia, *Tectonics,* vol. 15, pp. 1431–1446.

NABIGHIAN M N. & CORBETT J D. 1987 Resistivity Characteristics of Geologic Targets. pp. 1-5. SEG (Society of Exploration Geophysicists).

PAGE R. W.*, et al.* 2005 Correlation of Olary and Broken Hill Domains, Curnamona Province: possible relationship to Mount Isa and other northern Australian Pb–Zn–Ag-bearing successions, *Economic Geology,* vol. 100, pp. 663–676.

PALACKY G. J. 1993 Use of airborne electromagnetic methods for resource mapping, *Advances in Space Research,* vol. 13, no. 11, pp. 5-14.

ROACH I. 2012 The Frome airborne electromagnetic survey, South Australia*.*

ROACH I. C.*, et al.* 2018 Applied geophysics for cover thickness mapping in the southern Thomson Orogen, *Australian Journal of Earth Sciences,* vol. 65, no. 7-8, pp. 917-941.

ROBERTSON K., HEINSON G. & THIEL S. 2016 Lithospheric reworking at the Proterozoic–Phanerozoic transition of Australia imaged using AusLAMP Magnetotelluric data, *Earth and Planetary Science Letters,* vol. 425, pp. 27-35.

ROBERTSON K. & THIEL S. 2019 Detecting the Fingers of God: Optimising magnetotelluric survey design for mineral exploration, *ASEG Extended Abstracts,* vol. 2019, no. 1, pp. 1-3.

SCHNAIDT S. & HEINSON G. 2015 Bootstrap resampling as a tool for uncertainty analysis in 2-D magnetotelluric inversion modelling, *Geophysical Journal International,* vol. 203, no. 1, pp. 92-106.

SELWAY K. 2014 On the Causes of Electrical Conductivity Anomalies in Tectonically Stable Lithosphere, *Surveys in Geophysics,* vol. 35, no. 1, pp. 219-257.

SIMPSON F. & BAHR K. 2005 Practical Magnetotellurics*.* The Press Sindicate of the University of Cambridge, Cambridge.

SKIRROW R. G.*, et al.* 2018 Lithospheric Architecture and Mantle Metasomatism Linked to Iron Oxide Cu-Au Ore Formation: Multidisciplinary Evidence from the Olympic Dam Region, South Australia, *Geochemistry, geophysics, geosystems : G3,* vol. 19, no. 8, pp. 2673-2705.

TAMMEMAGI H. Y. & LILLEY F. E. M. 1973 A Magnetotelluric Traverse in Southern Australia, *Geophysical Journal of the Royal Astronomical Society,* vol. 31, no. 4, pp. 433–445.

THORKELSON D. J.*, et al.* 2001 Early Mesoproterozoic intrusive breccias in Yukon, Canada: the role of hydrothermal systems in reconstructions of North America and Australia, *Precambrian Research,* vol. 111, pp. 31–35.

TIKHONOV A. N. 1950 The determination of the electrical properties of deep layers of the Earth's crust, *Doklady,* vol. 73, no. 2, pp. 295-297.

VELLA L. & EMERSON D. 2009 Carrapateena: physical properties of a new iron-oxide copper-gold deposit, *ASEG Extended Abstracts,* vol. 2009, no. 1, pp. 1-13.

WADE C. 2011 Definition of the Mesoproterozoic Ninnerie Supersuite, Curnamona Province, South Australia, *MESA Journal,* vol. 62, pp. 25–42.

WADE C. E.*, et al.* 2012 Geochemistry and geochronology of the c. 1585Ma Benagerie Volcanic Suite, southern Australia: Relationship to the Gawler Range Volcanics and implications for the petrogenesis of a Mesoproterozoic silicic large igneous province, *Precambrian research,* vol. 206-207, pp. 17-35.

WANG L. J., LILLEY F. E. M. & CHAMALAUN F. H. 1997 Large-Scale Electrical Conductivity Structure of Australia from Magnetometer Arrays, *Exploration Geophysics,* vol. 28, no. 1-2, pp. 150-155.

WILLIAMS H. A. & BETTS P. G. 2009 The Benagerie Shear Zone: 1100 Myr of reactivation history and control over continental lithospheric deformation, *Gondwana Research,* vol. 15, no. 1, pp. 1-13.

YANG X. 2011 Origin of High Electrical Conductivity in the Lower Continental Crust: A Review, *Surveys in geophysics,* vol. 32, no. 6, pp. 875-903.

APPENDIX A: 3D MODEL SET UP AND FITS

The 3-D model presented in figure four involved Regional MT stations of 50 inversions the RMS was ~1, over a bandwidth from 10^{-1} – 10^{4} Hz. Error floors were set to 5%, cell sizes were set to 500 m to not over fit the inner mesh. Smoothing factor (tau) set as 0.01

in the vertical component and 2 for horizontal. Z_0 value in the vertical direction was set at 20 and 0 for horizontal.

The model does have limitations due to non-uniformity as the Curnamona Cube MT stations recorded only reach up to 100 Hz, while Jupiter stations up to 10000 Hz. Moreover, only a narrow frequency band can be assessed because the 3-D algorithm cannot accommodate all frequencies. Because of this imbalance in the density of data, there is an overload of information within the inner Jupiter array and a lack of information within the outer regions. To overcome this, a broad smoothing scale was applied which reduced the bunching of structures around MT stations. However, this inherently smoothed out structural features, ultimately masking anything on a small scale.

APPENDIX B: 2-D REGIONAL MODEL SET UP

This model was run over frequency range of 0.01 – 5,000 Hz, for 100 iterations to a RMS of 1.555. It fit 8 data points per decade, with noise floors for TM and TE Rho at 5% and TM and TE phase at 2.5%. Smoothing weight was set at 0.02, with horizontal to vertical smoothing at 1:2. Z0 was set at 5m and invert for static shift was set on, with a variance of 5% and damping set at 100. The model mesh was made up of 53975 cells, with 25km padding, and a padding factor of 1.5. The fits of phase invariant and invariant normalised to observed values are presented in the following figure.

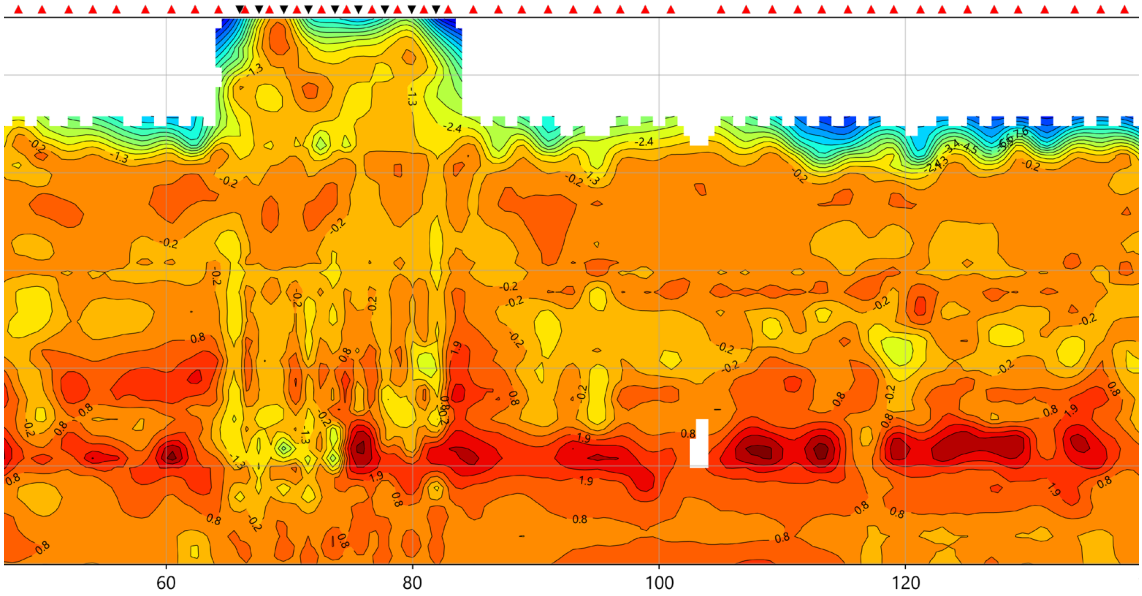

The figure below presents the modelled apparent resistivity invariant normalised by that of the observed data.

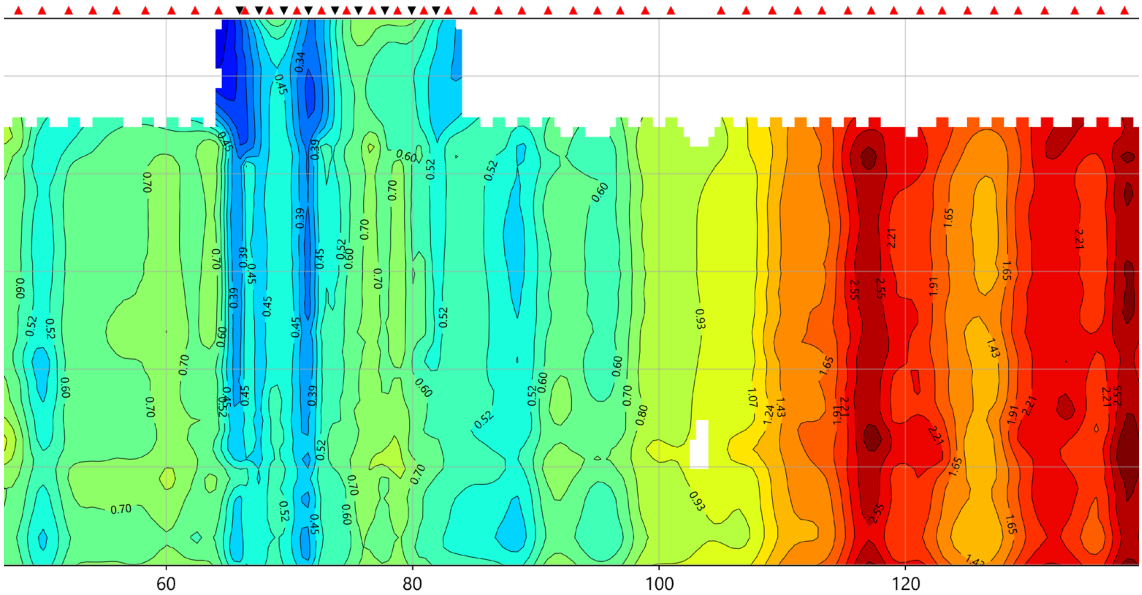

Appendix c: 2-D Jupiter profile models

2-D inversion models for each profile were run over the frequency range 0.01-5,000Hz, for 100 iterations. RMS values for profiles A, B, C, and D, were 1.070, 1.165, 1.012 and 1.191, respectively. All profiles were run using a mesh of more than 53,000 cells, fitting 8 points per decade. A priori model information was included, unique to each profile based on the 1-D inversion of the middle MT station. Horizontal-vertical smoothing was set 3:1, with Z_0 set at 5m and all 2-D models were inverted for static shift.

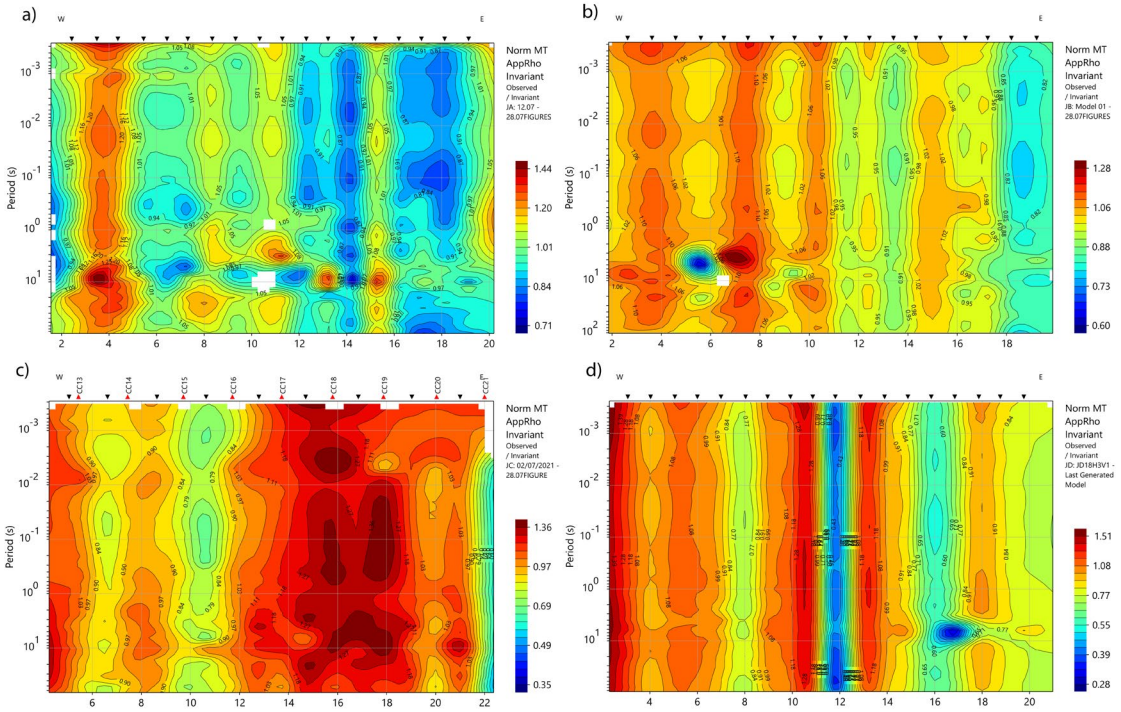

The next figure presents the phase invariant of each profile, normalised by that of the observed survey data.

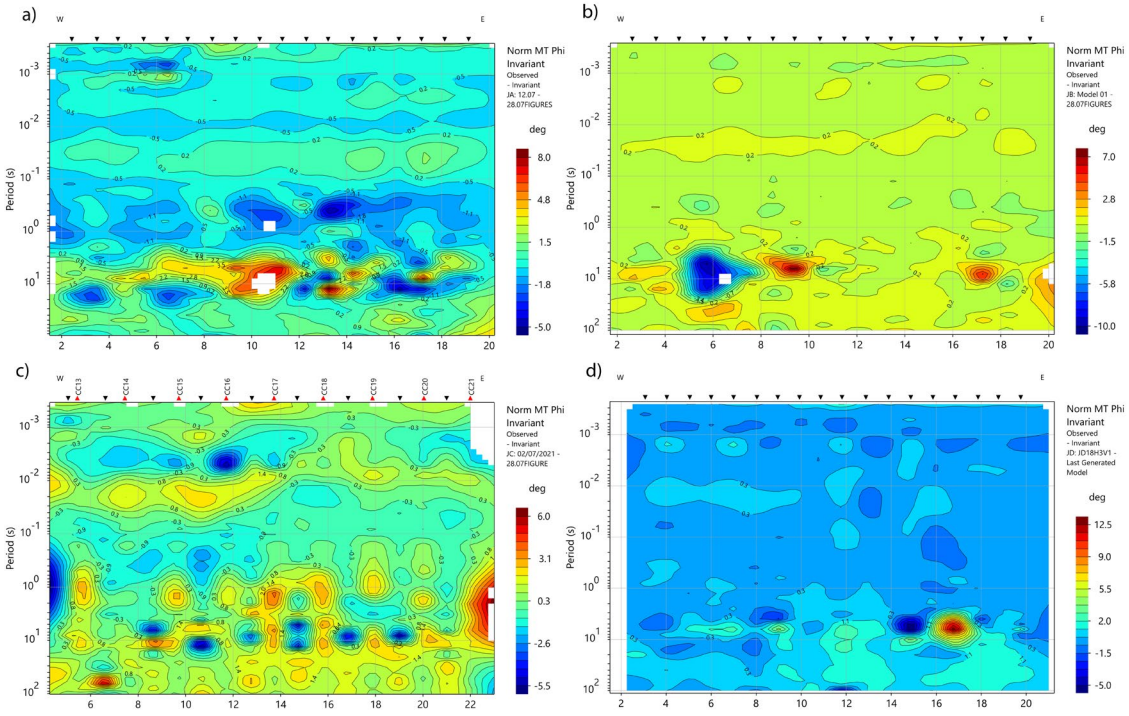

APPENDIX D: 1-D MODEL SET UP

A 1-D batch inversion was run using all Jupiter MT stations for a smoothed invariant with 15 layers per decade, from 10m to 40km. Noise floors for phase and apparent resistivity were set as 2.5% and 5%, respectively, with the observed curve set to invariant. The following figure present the apparent resistivity, normalised by the observed invariant at 3 and 30 s.

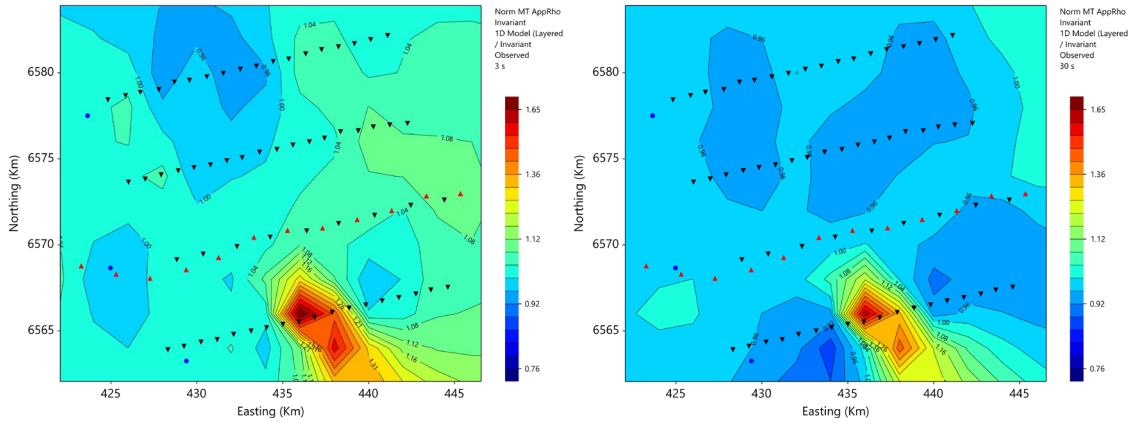

The following figure presents the phase invariant normalised by the observed phase invariant at 3 and 30 s.